ACS APPLIED MATERIALS & INTERFACES

www.acsami.org

Research Article

Dual-Wavelength Electrochemiluminescence Ratiometric Biosensor for NF-κB p50 Detection with Dimethylthiodiaminoterephthalate Fluorophore and Self-Assembled DNA Tetrahedron Nanostructures Probe

Zhenqiang Fan,[⊥] Zongqiong Lin,[⊥] Zepeng Wang, Jianfeng Wang, Minhao Xie, Jianfeng Zhao,* Kai Zhang,* and Wei Huang*

Cite This: *ACS Appl. Mater. Interfaces* 2020, 12, 11409−11418

Read Online

ACCESS | Metrics & More | Article Recommendations | Supporting Information

ABSTRACT: In this work, we fabricated a dual-wavelength electrochemiluminescence ratiometric biosensor based on electrochemiluminescent resonance energy transfer (ECL-RET). In this biosensor, Au nanoparticle-loaded graphitic phase carbon nitride (Au-g-C_3N_4) as a donor and Au-modified dimethylthiodiaminoterephthalate (TAT) analogue (Au@TAT) as an acceptor were investigated for the first time. Besides, tetrahedron DNA probe was immobilized onto Au-g-C_3N_4 to improve the binding efficiency of the transcription factor and ECL ratiometric changes on the basis of the ratio of ECL intensities at 595 and 460 nm, which were obtained through the formation of a sandwich structure of DNA probe−antigen−antibody. Our biosensor achieved the assay of NF-κB p50 with a detection limit of 5.8 pM as well as high stability and specificity.

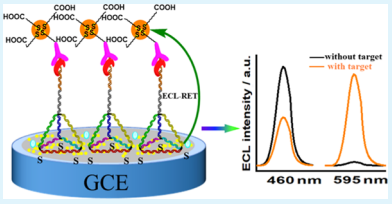

KEYWORDS: *dimethylthiodiaminoterephthalate (TAT), NF-κB p50, electrochemiluminescence, DNA tetrahedron nanostructures, ratiometric biosensor*

INTRODUCTION

Nuclear factor-kappa B (NF-κB) is a double-stranded DNA-binding transcription factor (TF), which plays an important part in enhancing or reducing a series of gene expressions involved in cell survival, proliferation, and differentiation, as well as cellular inflammation by recognizing and binding specific gene sequences.[1] The research on NF-κB is of great significance in cancer prevention associated with leukemias, breast, lung, brain, and so on.[2] The multicomponent quantitative detection of NF-κB is conducive in the development of anticancer therapeutic drugs and the clinical diagnosis of autoimmunity and inflammation.[3−5]

Traditional detection strategies for NF-κB are unable to meet people's requirements for speed, sensitivity, and simplicity. For example, the electrophoretic mobility shift assay (EMSA) is usually very time-consuming and the steps are cumbersome.[6] A DNA footprinting assay needs superb experimental skills and the operation is complicated.[7] The enzyme-linked immunosorbent assay (ELISA) is time-saving, simple, and easy to standardize.[8] However, it needs specific antibodies and is susceptible to false positives due to environmental factors such as temperature and time. The western blotting assay is usually expensive and increases the cost of the assay.[9,10] The immunohistochemistry assay has low sensitivity and is not convincing enough.[11] In recent years, the fluorescence assay has attracted people's wide attention due to its high sensitivity.[12] In the classic fluorescence assay the donor and acceptor bound with different DNA sequences induce fluorescence resonance energy transfer (FRET). However, DNA−protein binding produces steric hindrance which causes the contact between the donor and acceptor to be blocked, resulting in a weaker FRET signal.[13]

Compared to other technology, electrochemiluminesence (ECL) shows the advantages of high sensitivity, time saving, device available, owning a controllable reaction system, and possessing a broader detection range.[14−16] Owing to these characteristics, ECL technology is conducive to broadening the detection methods of TF in a sensitively selective way. Recently, ratiometric ECL methods which count on the ratio of the signals instead of the value of the signals have caught researchers' widespread attention for the reason that they can effectively eliminate the impact of the environmental factors on a single signal, which is meaningful to strengthen the ability to resist the surrounding interference using an ECL strategy in biomedical analysis.[17,18] For ratiometric ECL methods, dual-potential and dual-wavelength ratio modes are included. Dual-

Received: January 21, 2020
Accepted: February 18, 2020
Published: February 18, 2020

potential mode is already widely used in the detection of prostate-specific antigen (PSA), aflatoxin B1 (AFB1), dopamine, miRNA, metal cation, and cancer cells.[19−24] However, dual-wavelength mode is restricted by the emitting intensity and the wavelength of the emitter; the common dual-wavelength ECL system is graphitic phase carbon nitride (g-C_3N_4) and $Ru(bpy)_3^{2+}$.[25,26] Therefore, the exploration of luminescent materials with splendid ECL emitting intensity and appropriate wavelength becomes the key to expanding the dual-wavelength biosensors.

In a ratiometric ECL strategy, electrochemiluminesence-resonance energy transfer (ECL-RET) is extensively employed in the creation of biosensors, the basic condition of which is spectral overlap between the donor and the corresponding acceptor in close contact.[27,28] Herein, we employed a dual-wavelength ECL ratiometric strategy for the detection of NF-κB with gold-doped g-C_3N_4 (Au-g-C_3N_4) nanosheets as a donor and reduced-gold modified dimethylthiodiaminoterephthalate (TAT) fluorophore (Au@TAT) as an acceptor, owing to the donor's ECL emission wavelength (460 nm), which is consistent with the acceptor's absorption wavelength. g-C_3N_4 is an excellent semiconductor nanomaterial with outstanding biocompatibility and luminous efficiency, so, it is widely used in the determination of miRNA, cardiac troponin, cancer cells, and so on.[29−31] TAT fluorophore with a strong intramolecular distortion structure results in a high quantum efficiency of 54.44%, which can effectively suppress charge transfer and improve radiation transition efficiency.[32] Moreover, such TAT compound with a longer emission wavelength of approximately 595 nm will improve the penetration of light and reduce energy loss to good effect, which is of great value in biometric applications.[33] For the outstanding optical properties and biostability, g-C_3N_4 and TAT are served as a constructor of ECL-RET. To enhance the ECL intensity and the intrinsic conductivity of the original material, Au nanoparticles are introduced to modify them. The formation of Au-g-C_3N_4 also facilitates the immobilization of nucleic acid probes and Au nanoparticles on the surface of the TAT compound and increases the loading amount of antibody which is conducive to raising the efficiency of the reaction. However, ECL-RET signals are susceptible to be affected by the adsorption of binding proteins or capturing antibodies, as well as the uneven distribution of proteins on the surface of the electrode for the changes of interface conductivity.[34] Therefore, there is an urgent need to overcome the obstacles.

To conquer the difficulties, robust and simplest nucleic acid probes on the electrode that can resist the interference of the cell enzyme are needed. The development of DNA nanotechnology not only enables DNA structures to be highly predictable and programmable with extremely precise size and well-defined geometry characteristics, but also realizes the functional requirements such as the detection of pH, $O_2^{\bullet-}$, miRNA, and DNA methylation when modified with small molecules.[35−37] Among miscellaneous DNA nano architectures, three-dimensional (3D) DNA tetrahedron nanostructures (DTNs) synthesized by the self-assembly of four single strands of DNA attract people's widespread concern for its high structural stiffness.[38] DTNs with the characteristics of simple synthesis and predictable dimensions will reduce the crowdedness, uneven distribution, and cross-reactivity of single- or double-stranded probes on the surface of electrodes, thereby, improving the biorecognition pathway and lessening the nonspecific absorption.[39−41] The vertex of DTNs can be modified by various functional biomolecules or special binding nucleic acid sequences to realize the expansion from traditional 1D and 2D DNA probes to 3D multiple probes.[42−45]

Here, a dual-wavelength electrochemiluminescence ratiometric biosensor with self-assembled DTNs was fabricated for selective and ultrasensitive determination of NF-κB p50. In this study, the donor (Au-g-C_3N_4) and the acceptor (Au@TAT) exhibited a very high resonance energy transfer efficiency, and the ratio of ECL intensities at 595 and 460 nm had a linear relationship with the logarithmic value of NF-κB p50 concentration. Most importantly, the dual-wavelength ratiometric biosensor can achieve the detection of NF-κB with high sensitivity and reproducibility in diluted cell nuclear extracts.

EXPERIMENTAL SECTION

Reagents and Materials. Gold chloride hydrate ($HAuCl_4 \cdot xH_2O$), sodium borohydride, acetic acid, citrate sodium, sodium borohydride, 1-ethyl-3-(3-dimethyllaminopropyl)-carbodiimide hydrochloride (EDC), and *N*-hydroxysuccinimide (NHS) were obtained from Aladdin Biochemical Technology Co. Ltd. (Shanghai, China). Ethylene diamine tetraacetic acid (EDTA) and triethylamine were obtained from Sinopharm Chemical Reagent Co. Ltd. (Shanghai, China). Trisodium citrate dihydrate and silver nitrate were obtained from Sigma. Dimethyl 2,5-dioxocyclohexane-1,4-dicarboxylate was obtained from Energy Chemical (Shanghai, China). 3-(Methylthio)aniline and pluronic P123 were obtained from Bidepharm (Shanghai, China), and Heowns (Tianjin, China), respectively. NF-κB p50 (human recombinant) was obtained from Hengfei Biotechnology Co. Ltd. (Shanghai). Threo-1,4-dimercapto-2,3-butandiol (DTT), 6-mercaptohexan-1-ol (MCH), tris(2-carboxyethyl) phosphine hydrochloride (TCEP), NF-κB p50 antibody, and phosphate-buffered saline (PBS) buffer solution were obtained from Sangon Biotech Co. Ltd. (Shanghai). The water was purified by the Milli-Q purification system (Branstead). Purified oligonucleotides were available from Genscript Bio-technology Co. Ltd. (Nanjing, China), and the sequences of DTNs are depicted in Table S1.

Apparatus. Scanning electron microscopy (SEM) and energy-dispersive X-ray (EDX) images were obtained by JSM-7800F (Japan). Transmission electron microscope (TEM) images were obtained from 1400 PLUS (Japanese electronics). ECL signals were detected by ECL-6B provided by State Key Laboratory of Analytical Chemistry for Life Science, Nanjing University. ECL experiments were tested by a three-electrode system containing a glassy carbon electrode (GCE), platinum counter electrode, and Ag/AgCl reference electrode. UV−vis spectra were analyzed by Spectra Max M5e (Molecular Devices Co. Ltd). Single-crystal structure data were measured by Bruker D8 venture. ^{1}H NMR spectra (NMR) were obtained using an NMR spectrometer (Bruker 400 MHz). Atomic force microscope images were obtained from Dimension ICON (Bruker).

Synthesis and Purification of the Illuminator (TAT). The mixture of dimethyl 2,5-dioxocyclohexane-1,4-dicarboxylate (2.28 g, 10 mmol) and 3-(methylthio)aniline (3.02 mL, 25 mmol) was added into ethanol/glacial acid (20 mL:10 mL) and heated at 90 °C in a one-neck flask for 5 h with a magnetic stir bar. After the reaction, the mixture was treated with vacuum filtration. Then the crude product was collected, washed as orange-red powder, and purified by column chromatography with dichloromethane and petroleum ether as the eluents. Finally, 3.03 g of TAT was obtained with 75.3% yield. ^{1}H NMR (400 MHz, $CDCl_3$) δ = 8.02 (s, 2H), 7.25−7.21 (m, 4H), 7.07 (s, 2H), 6.94−6.89 (m, 4H), 3.86 (s, 6H), 2.48 (s, 6H).

Preparation of Au-g-C_3N_4. We synthesized Au-g-C_3N_4 successfully, and the method is specified as follows. First, we added 40 μL of $HAuCl_4 \cdot xH_2O$ (0.01 mM) solution to 4 mL carbonitride ethanol−water dispersion (15 mg L^{-1}) and the mixture was stirred it at room temperature for 4 h to get a mixture solution of g-C_3N_4 and $HAuCl_4$. Secondly, 30 μL of freshly prepared $NaBH_4$ (0.2 M) solution was injected into the mixture under an ice bath condition and stirring was continued for 30 min. Finally, 30 μL of sodium citrate (0.02 M) was

https://dx.doi.org/10.1021/acsami.0c01243
ACS Appl. Mater. Interfaces 2020, 12, 11409−11418

Scheme 1. Schematic Illustration of a Ratiometric ECL Immunosensor for the Transcription Factor (NF-κB p50) Assay

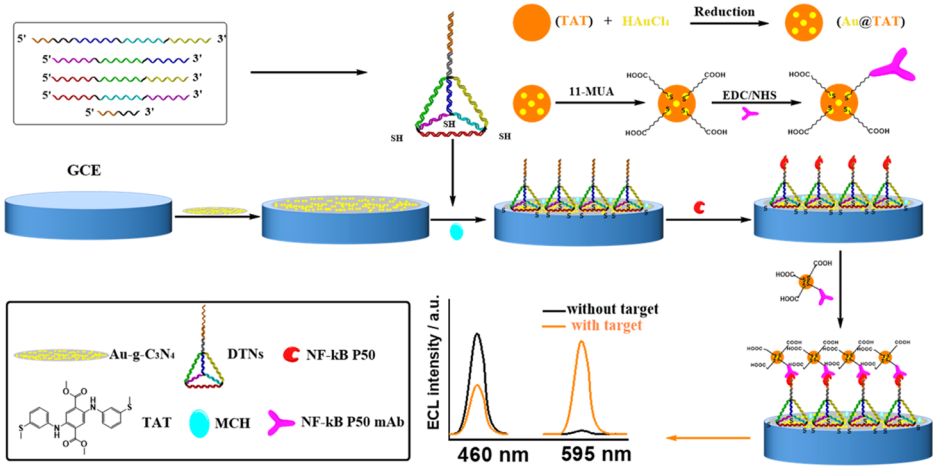

added and stirring was continued for another 30 min; then the mixture was centrifuged at 12 000 rpm for 1 min. After being washed with ultrapure water twice, the precipitant was dissolved in 5 mL of ultrapure water to get Au-g-C_3N_4, and then it was stored in a refrigerator at 4 °C for further use.

The Synthesis of Au@TAT Nanocomposites. We successfully modified TAT with the Au element to obtain Au@TAT nanocomposites by referring the methods in the literature presented previously.[46] For their preparation, first of all, we prepared 5 mL of TAT tetrahydrofuran (2 mg mL^{-1}) solution by stirring and ultrasonic dispersion. Under the stirring condition, they were injected into 50 mL of prepared pluronic p123 (1 mg mL^{-1}) solution. Simultaneously, 300 μL of $HAuCl_4{\cdot}xH_2O$ (0.01 M) solution was added into the mixture. Shortly after that, 400 μL of sodium citrate (0.01 M) was dropped quickly when the mixture was heated to the boiling point. After waiting for 15 min, we turned off the heater and cooled it to room temperature. Then centrifugation and washing were carried out to get Au@TAT nanocomposites, which were dissolved in 10 mL of ultrapure water and, finally, stored in a refrigerator at 4 °C for future use.

Preparation of ECL Biological Probe. To prepare the biological probe (mAb-Au@TAT), Au@TAT nanocomposites were first modified with carboxylic acid group referring to the previously reported literature.[47] In short, 5 mL of 11-mercaptoundecanoic acid (2.4 mM) ethanol solution and 5 mL of sodium hydroxide (2.4 mM) aqueous solution were added to the 5 mL of prepared Au@TAT solution. Then the mixture was stirred at 80 °C for 1 h. When the mixture cooled to room temperature, it was centrifuged (12 000 rpm) for 10 min and washed by ultrapure water two times for further use. After that, the biological probe (mAb-Au@TAT) was prepared referring to the EDC-NHS method.[34] First, 250 μL of EDC (0.5 M) solution was added into 1 mL of carboxylated Au@TAT (COOH-Au@TAT) aqueous solution under agitation for 1 h at room temperature. Next, 250 μL of NHS (0.5 M) and 100 μL of NF-κB p50 antibody (mAb) (1 mg mL^{-1}) were dropped; then the mixture solution was put in a refrigerator and reacted overnight at 4 °C. After that, the reaction solution was poured into a Nanosep Centrifugal 30 K Devices and centrifuged at 12 000 rpm for 20 min at 4 °C. Finally, the mixture was diluted to 200 μL for further utilization.

Preparation of DTNs and Polyacrylamide Gel Electrophoresis (PAGE). DTNs were prepared as follows. First, strands of T_1, T_2, T_3, T_4, and T_5 with the final concentration of 1 μM, respectively, were dispersed in the phosphate buffer (pH 7.4) containing 5.0 mM $MgCl_2$ and 0.1 mM TCEP, and incubated for 40 min at room temperature under agitation. Then the mixture was heated to 95 °C and immediately cooled down to 4 °C for forming the sturdy DTNs which had been stored in a refrigerator for further use.

After that, the successful formation of DTNs was verified by nondenaturing PAGE (15%), which was carried out in 1× TBE (89 mM Tris-boric-acid, 2 mM EDTA, pH 7.4) buffer at a constant voltage of 110 V for 2.5 h at 25 °C. Then the gels were stained with ethidium bromide (EB) for 20 min and photographed by UV light (ChemiDoc MP, Bio-Rad).

Fabrication of the ECL Ratiometric Biosensor. To fabricate the ECL biological biosensor, the GCE was needed to be polished by 0.05 μm Al_2O_3 powder initially. In addition, it was immersed into ultrapure water containing 0.1 M H_2SO_4 and 0.2 M H_2O_2; then the adsorbed substance was ultrasonically cleared afterward. After being washed with ultrapure water and ethanol, it was dried in clean air for further application. Then 8 μL of Au-g-C_3N_4 suspended solution was dropped on the spotless electrode and dried for 50 min in the clean air to form Au-g-C_3N_4/GCE. Next, it was dipped in DTN (1 μM) phosphate solution for 12 h to constitute the DTN-modified Au-g-C_3N_4 biosensor architecture by the Au−S bond. After that, it was immersed in 2 mM MCH phosphate (pH 7.4) solution for 40 min at room temperature to passivate the unoccupied sites of the electrode. Then, various concentrations of NF-κB p50 in a protein incubation solution, which contained Tris−HCl (10 mM, pH 7.4), DTT (300 μM), 5% glycerol, and EDTA (100 μM), were incubated with the modified electrode for 50 min at room temperature. The incubation of NF-κB p50 in diluted cell nuclear extracts was implemented in the protein incubation solution as well. In the end, 8 μL of biological probe (mAb-Au@TAT) was dropped on the electrode and kept for 1 h at room temperature. ECL measurements were carried out at the potential scan of −1.6−0 V in a phosphate (pH 7.4) solution containing 0.1 M $K_2S_2O_4$. Last but not least, it was essential to be cleaned by the phosphate (pH 7.4) solution for every step of modification of the electrode.

Cell Culture and Cell Nuclear Extract Preparation. According to previous reports, we put cell culture and cell nuclear extract preparation into execution.[48] First of all, A549 cells were cultured in Dulbecco's modified eagle medium (DMEM; GIBCO) in the presence of 10% fetal calf serum, penicillin (0.1 g L^{-1}), and streptomycin (0.1 g L^{-1}) under humid atmosphere consisting of 5% CO_2.

A total of 5×10^7 cells, as calculated by the Petroff-Hausser cell counter, were first washed by the phosphate (pH 7.4) solution at 0 °C. Then 20 ng mL^{-1} of TNF-α (Pepro Tech) was added to the cells and allowed to incubate for 30 min. Next, the cell nuclear extracts were collected by the nuclear extract kit (Active Motif, Carlsbad, CA) in the light of the instructions of the manufacturer. After that they were diluted to 200 μL and then stored immediately at −80 °C for use.

https://dx.doi.org/10.1021/acsami.0c01243
ACS Appl. Mater. Interfaces 2020, 12, 11409−11418

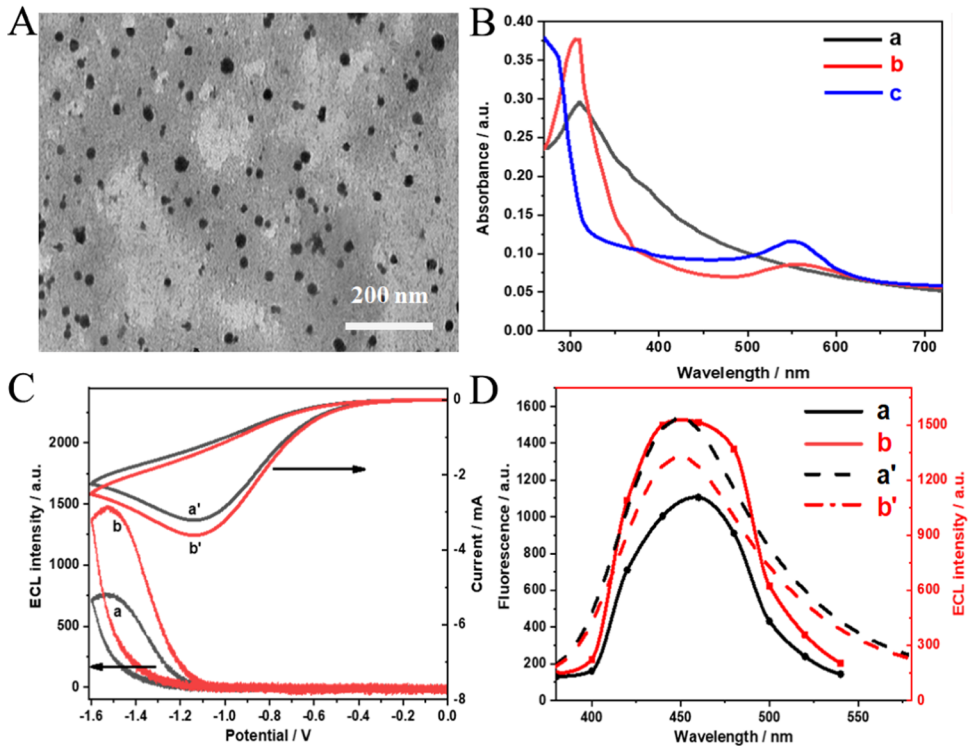

Figure 1. (A) TEM image of Au-g-C_3N_4. (B) The UV−vis absorption spectra of (a) g-C_3N_4, (b) Au-g-C_3N_4, and (c) Au nanoparticles. (C) ECL intensity of (a) g-C_3N_4 and (b) Au-g-C_3N_4, and the corresponding CV curves of (a′) g-C_3N_4 and (b′) Au-g-C_3N_4. (D) ECL spectra of (a) g-C_3N_4 and (b) Au-g-C_3N_4, which were gained through a series of optical filters and fluorescence spectra of (a′) g-C_3N_4, (b′) Au-g-C_3N_4 with the 310 nm excitation.

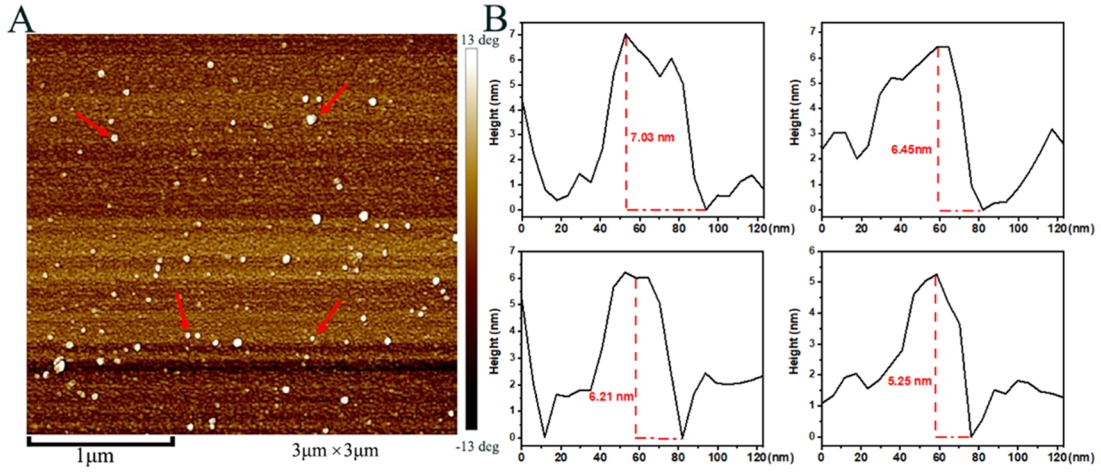

Figure 2. (A) Characterization of DTNs with atomic force microscopy. (B) Height profiles of DTNs marked with a red arrow in (A).

RESULTS AND DISCUSSION

Principle of the Proposed Dual-wavelength Ratiometric ECL Biosensor. As shown in Scheme 1, the donor (Au-g-C_3N_4) complex was arranged on the surface of the carbon glassy electrode through electrostatic adsorption. Then DTNs were modified onto the Au-g-C_3N_4 complex through the Au−S bond and MCH was added to block the nonspecific adsorption sites. Meanwhile, the acceptor (Au@TAT) was modified by carboxylic acid group to further connect with the NF-κB p50 antibody to prepare the biological probe (mAb-Au@TAT) using the EDC-NHS method. NF-κB p50 was bound to the special binding nucleic acid sequence at the stem of the DTNs by protein−dsDNA binding activity.[49,50] After that the dsDNA-TF-antibody sandwich structure was formed with the arrival of the biological probe. This formation triggers the energy transfer with the ECL-RET signal recorded in the presence of co-reactant $K_2S_2O_4$. Therefore, a dual-wavelength ratiometric ECL biosensor for the assays of NF-κB p50 was successfully fabricated.

Characterization of Au-g-C_3N_4. To get the structure and the size of Au-g-C_3N_4, the TEM image was taken, as depicted in Figure 1A. From the TEM image, we could see that g-C_3N_4 had a sheet-like morphology. Besides, the synthesized Au nanoparticles were homogeneously distributed on the surface of g-C_3N_4 and the size was around 25 nm. The UV−vis spectra were used to further confirm the structure, as shown in Figure

https://dx.doi.org/10.1021/acsami.0c01243
ACS Appl. Mater. Interfaces 2020, 12, 11409−11418

1B. They showed that g-C_3N_4 had an absorption peak (curve a) at 310 nm. However, not only did Au-g-C_3N_4 (curve b) exhibit a characteristic absorption peak of g-C_3N_4, but it also showed the absorption peak at 540 nm, which should be attributed to Au nanoparticles (curve b) of specific size dispersed on the g-C_3N_4 surface. The introduction of Au NPs was to improve the conductivity of g-C_3N_4 and thus enhance the luminous intensity. It was also essential to verify the electrochemical effect of Au-g-C_3N_4. As depicted in Figure 1C, the ECL response of Au-g-C_3N_4 (curve a) was greatly enhanced compared to that of g-C_3N_4 (curve b), as Au nanoparticles played an electrocatalytic role in the reduction of $S_2O_8^{2-}$. Meanwhile, the corresponding cyclic voltammetry (CV) curve also verified the results that Au-g-C_3N_4 (curve a′) facilitated charge conduction compared to g-C_3N_4 (curve b′). Figure 1D indicates that ECL spectra (curves a and b) near 460 nm were slightly red-shifted compared to fluorescence spectra (curves a′ and b′). The loading of Au nanoparticles could increase the ECL intensity due to improvement in the efficiency of electron transfer, but cause a slight decrease in the fluorescence intensity for self-absorption.

Characterization of DTNs. Atomic force microscopy (AFM) images were performed to prove the well-dispersed DTNs. As depicted in Figure 2A, the AFM image showed that the DTNs had unanimous sizes. For the length of per base pair is 0.34 nm, the height of DTNs was calculated as 4.72 nm and the side length was 5.78 nm. However, the base pairs on the stem of DNA tetrahedron would increase the height and the length according to the actual nanostructure. The height distribution of DTNs (Figure 2B) was ranged 5.25−7.03 nm, which was higher than the theoretical height and the side length of DNA tetrahedron. This was due to the actual nanostructure of DTNs that the base pairs of the stem except that on the edge of the tetrahedron caused a slight deviation from the theoretical value. The formation of DTNs was also characterized by native PAGE as depicted in Figure S2. The ssDNA T1 (lane 1) was used as a reference band. Lanes 2, 3, and 4 were the partial hybridization of T1 with T2, T3, and T4, respectively, which led to bright stripes. Lanes 5 and lane 6 indicated that with the gradual assembly of tetrahedron, the migration speed of the strips became slower. In a word, we could infer that with the increasing number of ssDNA from T1 to T5, the stripes migrated slowly gradually and the DTN (lane 7) band migrated the most slowly compared with the other combinations of ssDNA. As the DTN band was single and bright, we could conclude that DTNs were successfully formed and the purity was high.

Characterization of Au@TAT Nanocomposites. SEM images were taken to characterize the morphologies and structure of the as-synthesized TAT nanoparticles and Au@TAT nanocomposites. As depicted in Figure 3A, we observed that the as-synthesized TAT nanoparticles were uniformly dispersed in an aqueous solution at the size of approximately 100 nm after emulsification treatment. When Au^{3+} was reduced on the surface of TAT nanoparticles, the image with great difference compared to TAT nanoparticles was showed in Figure 3B. From the image, we find that the nanocomposites at 250 nm became more transparent than TAT nanoparticles, owing to the fact that Au nanoparticles were grown on the surface of TAT nanoparticles. Dynamic lighting scattering (Figure S7) showed similar results for TAT at the size of approximately 95 nm and Au@TAT at around 230 nm. The result was further confirmed by EDX. As shown in Figure 3C,

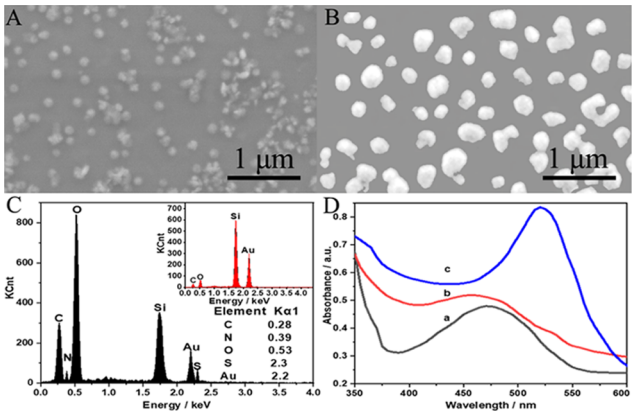

Figure 3. SEM images of (A) as-synthesized TAT and (B) Au@TAT nanocomposites. (C) The EDS spectra of Au@TAT; inset spectra of Au nanoparticles. (D) The UV−vis absorption spectra of (a) as-synthesized TAT, (b) Au@TAT nanocomposites, and (c) Au nanoparticles in the aqueous solution.

obvious N (0.39 keV) and S (2.3 keV) peaks were observed in Au@TAT nanocomposites compared to Au nanoparticles (inset of Figure 3C). What is more, the increase in the peaks of the C and O elements (0.28 and 0.53 keV) in Au@TAT nanocomposites was detected clearly. Apart from that, UV−vis spectra (Figure 3D) were also used to verify the result. Compared with the spectra of as-synthesized TAT, the spectra of Au@TAT nanocomposites showed a new absorption band at 525−535 nm, which were ascribed to the grown Au nanoparticles on the surface. Therefore, all these pieces of evidence verified that Au@TAT nanocomposites were successfully prepared. Elemental mapping analyses were further performed to characterize the element distribution of Au@TAT. As expected, TAT with the main elements of carbon (Figure 4B), nitrogen (Figure 4D), and sulfur (Figure 4E) was

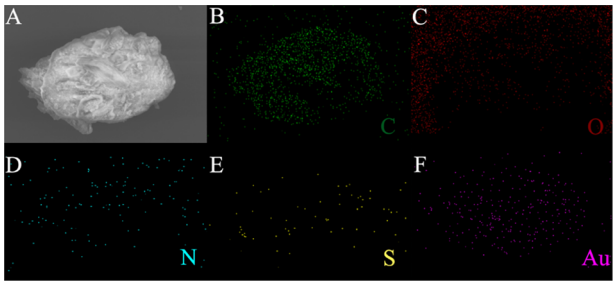

Figure 4. SEM image of one Au@TAT nanoparticle (A). Elemental mapping analyses of C (B), O (C), N (D), S (E), and Au (F).

observed. The oxygen element (Figure 4C) was identified for the use of surfactant P123 in the synthesis process. As shown in Figure 4F, most Au^{3+} was reduced homogeneously on the surface of as-synthesized TAT to form Au-coated nanocomposites. It confirmed that the decoration of TAT was completed successfully. Then, the surface of Au@TAT was modified with carboxylic acid group, and the normalized UV−vis absorption spectra and fluorescence spectra of Au@TAT and Au@TAT modified with carboxylic acid group (COOH-Au@TAT) are depicted in Figure S4. This showed that the modification of carboxylic acid did not affect absorption and emission. Thus COOH-Au@TAT could be used for the next modification.

https://dx.doi.org/10.1021/acsami.0c01243
ACS Appl. Mater. Interfaces 2020, 12, 11409−11418

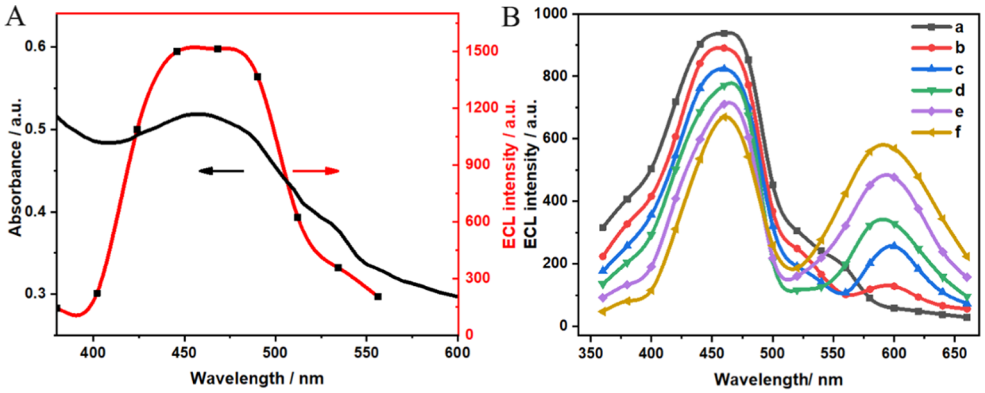

Figure 5. (A) UV−vis absorption of Au@TAT (a) and the ECL spectrum of Au-g-C_3N_4 (b). (B) ECL emission of the ratiometric biosensor in different NF-κB p50 concentrations (0, 10, 100, 1000, 10 000, 50 000 pM from a to e). The ECL spectra were individually measured through a series of optical filters (320−660 nm spaced 20 nm) in the 0.1 M PBS buffer solution (pH 7.4) containing 0.1 M $S_2O_8^{2-}$.

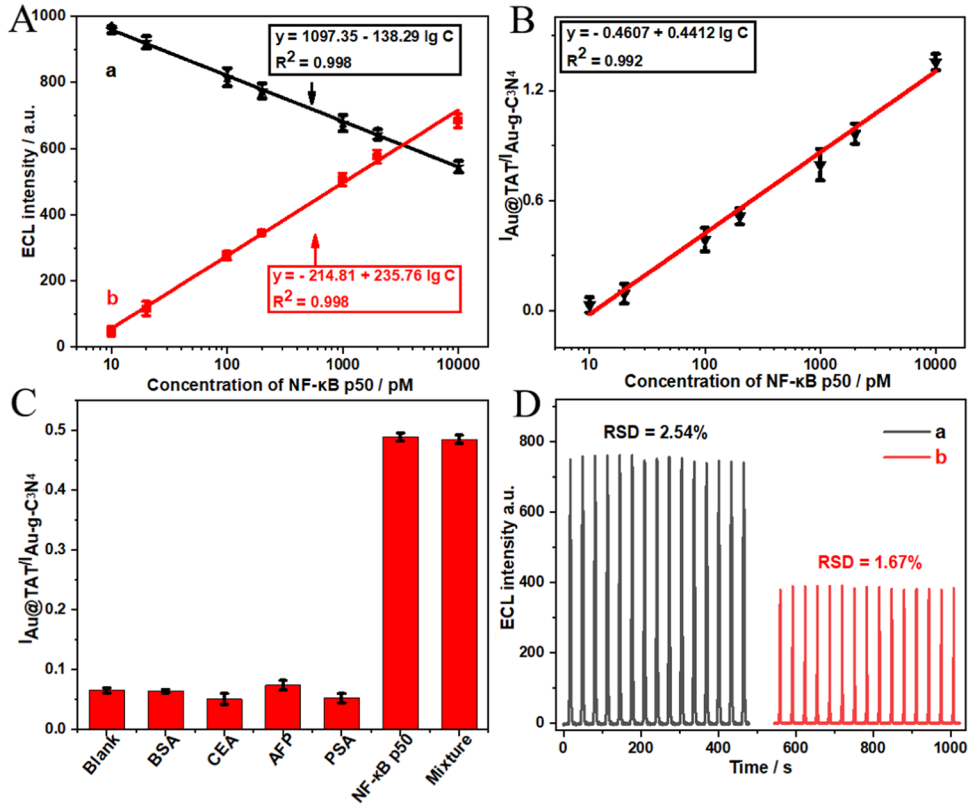

Figure 6. (A) Relationship between the ECL responses of (a) Au-g-C_3N_4 at the wavelength of 460 or (b) Au@TAT at the wavelength of 595 nm and the logarithm of NF-κB p50 concentrations (10, 20, 100, 200, 1000, 2000, 10 000 pM) with five independent duplicate measurements. (B) Relationship between the ratio of ECL intensity of Au@TAT to that of Au-g-C_3N_4 and the logarithm of NF-κB p50 concentrations. (C) The specificity of the ECL ratiometric biosensor against NF-κB p50 (100 pM) and nonspecific proteins (1 nM). (D) ECL reproducibility of (a) Au-g-C_3N_4 and (b) Au@TAT with 1000 pM NF-κB p50 under 15 successive cycles of cyclic potential. The assays were carried out in the PBS buffer solution (0.1 M, pH 7.4) containing 0.1 M $S_2O_8^{2-}$.

Characterization of the Modified Electrode. For the stepwise modification of the electrode, CV, electrochemical impedance spectroscopy (EIS), and the ECL response were utilized to characterize the surface features. The bare electrode showed a reversible redox (Figure S5A, curve a). With Au-g-C_3N_4 deposited on the electrode, the redox peak decreased obviously (curve b). After DTNs (curve c), MCH (curve d), and NF-κB p50 (curve e) were successively immobilized onto the Au-g-C_3N_4-modified electrode. The redox peak continued to decline, which was attributed to the impedance of electron transfer caused by a nonconducting substance on the electrode. However, when mAb-Au@TAT was attached on the modified electrode (curve f), an increase of the redox peak was observed significantly for the excellent conductive ability of mAb-Au@TAT. As shown in Figure S5B, the complex impedance was expressed as the sum of real Z' and imaginary Z'', which chiefly came from the cell's resistance and capacitance, separately. The model circuit as a modified Randles circuit was chosen cautiously to fit precise values to reveal the appropriate electrochemical process. The circuit consisting of the electro-

https://dx.doi.org/10.1021/acsami.0c01243
ACS Appl. Mater. Interfaces 2020, 12, 11409−11418

lyte's ohmic resistance (R_s), and the resistance of charge transfer (R_{ct}) connected with Warburg (W) diffusion impedance, and then in parallel with the constant phase element (CPE), is related to the double layer and reflects the interface of the membrane with the electrolyte solution. R_s is presented as the resistance of the working electrode and reference electrode. R_{ct} mainly accounting for the interfacial resistance through the high-frequency semicircle of the Nyquist diagram depends on the charge transfer kinetics of the redox reaction, and the value reveals the conductivity of the surface layer. CPE is served as a nonlinear capacitor, reflecting the inhomogeneity of the film. W corresponds to the limited ion diffusion possibly caused by molecular motion by ion conduction. It was observed that, with the stepwise modification of the electrode, R_{ct} was gradually increasing from a to e. When mAb-Au@TAT was immobilized on the electrode, the $R_{ct}$was decreased significantly. Therefore, we could infer that the actual R_{ct} corresponded to different modification stages of the proposed biosensor. ECL emission (Figure S5C) was also investigated; when Au-g-C_3N_4 (curve b) was dropped on the electrode, ECL emission with high intensity appeared. After DTNs (curve c), MCH (curve d), NF-κB p50 (curve e) were assembled one after another, there was a slight decrease in the ECL intensity. While mAb-Au@TAT (curve f) was attached, the ECL intensity was significantly raised, indicating that mAb-Au@TAT was successfully modified. Electrochemical and ECL changes of the electrode confirmed that dual-wavelength ratiometric biosensor was fabricated successfully.

ECL-RET Mechanism of the Ratiometric Biosensor. The ratiometric biosensor was based on ECL-RET between Au-g-C_3N_4 and Au@TAT. As Figure 5A shows the UV−vis spectra of Au@TAT and the ECL emission spectra of Au-g-C_3N_4. The overlap of the maximum spectra centered at 460 nm verified the occurrence of ECL-RET. ECL spectra at different concentrations of NF-κB p50 were also investigated by a series of optical filters, which are depicted in Figure 5B. In the absence of NF-κB p50, the emission peak of Au-g-C_3N_4 at 460 nm was merely detected (curve a). However, as the NF-κB p50 concentrations increase, the emission peaks of Au@TAT at 595 nm were continuously increased, which were accompanied by the obviously continuous decline of the ECL intensity of Au-g-C_3N_4 (curves b to e) owing to ECL-RET. Moreover, the ECL emission scanned at cathodic potential from −1.6 to 0 V is shown in Figure S3. The Au@TAT-modified GCE exhibited a feeble ECL response in the cathodic ECL system, indicating that Au@TAT was not used as an ECL emitter in cathodic potential. However, Au-g-C_3N_4-modified electrode under the same test condition showed excellent ECL intensity in the presence of $S_2O_8^{2-}$, and the ECL mechanism was described in previous reports.[51] So, Au-g-C_3N_4 was used as an emitter and Au@TAT regarded as an acceptor in this ratiometric biosensor. All these pieces of evidence verified the efficiency and feasibility of ECL-RET between Au-g-C_3N_4 and Au@TAT.

Analytical Performance of the Ratiometric Biosensor. As depicted in Figure 6A, with the increasing concentration of NF-κB p50, the ECL intensity of Au-g-C_3N_4 became smaller and the intensity of Au@TAT became larger, which indicated that NF-κB p50 facilitated the immobilization of Au@TAT to form a sandwich structure based on ECL-RET. To get an excellent ECL reliability, we used the ratiometric method to detect NF-κB p50 by calculating the ratio of ECL intensities of $I_{Au@TAT}$ and $I_{Au\text{-}g\text{-}C_3N_4}$. The ratio was linearly dependent on the logarithmic value of NF-κB p50 in the concentration range from 10 pM to 10 nM with R^2 = 0.992 (Figure 6B). In addition, the ECL-RET efficiency defined as I_E was calculated by $1 - I/I_0$ and referred to as the quenching efficiency, where I and I_0 are the ECL intensities at 460 nm with and without NF-κB p50, respectively. The ECL-RET efficiency with a good linear relationship is shown in Figure S6A. Meanwhile, the comparison of the ECL-RET efficiency in response to ssDNA and DTN probe-based biosensors with or without MCH passivation was made, as shown in Figure S6B. MCH passivation was an important treatment step on the surface of electrodes modified with the linear DNA probe. The DTNs-based biosensor had higher ECL-RET efficiency than the ssDNA/MCH-based sensors, which was attributed to the similarly splendid orientation of DTNs on the electrodes, avoiding entanglement between soft ssDNA probes. As a consequence, the DTNs-based biosensor was more sensitive than ssDNA-based sensors and more suitable for the assays of NF-κB p50. Last but not most, the detection method exhibited a detection limit (LOD) as low as 5.8 pM based on the 3σ rule. In addition, the LOD of the proposed ratiometric biosensor was comparable and the detection range was wider compared with the previously reported methods (Table S2).

Specificity and Reproducibility of the Ratiometric Biosensor. Four nonspecific proteins were selected as interference proteins, including bovine serum albumin (BSA), carcinoembryonic antigen (CEA), a-fetoprotein (AFP), and PSA, as well as the mixture of NF-κB p50 and nonspecific proteins. They were utilized to assess the specificity of the ratiometric biosensor under the identical assay condition. As depicted in Figure 6C, NF-κB p50 and the mixture of NF-κB p50 with other nonspecific proteins had almost the same response. Obviously, there were differences between the target protein and the nonspecific proteins which had a similar result with the blank sample, emphasizing the remarkable specificity of the ratiometric biosensor. The reproducibility was estimated by the continuous potential scanning of 20 cycles with 400 pM NF-κB p50 (Figure 6D). The relative standard deviations (RSD) of Au-g-C_3N_4 and Au@TAT were 2.54 and 1.67%, respectively, revealing the prominent stability of the ECL assay system.

Sample Determination. For further verifying the application of the proposed ECL ratiometric biosensor, the assays were applied in the detection of NF-κB p50 in 10 diluted nuclear extracts. As depicted in Table 1, the concentration of 0 pM in diluted nuclear extracts was detected to be 65.5 pM. Besides, the recovery rate and relative standard deviation (RSD) were used to illustrate the accuracy of the

Table 1. Determination of NF-κB p50 in 10-Fold Diluted Nuclear Extracts

		NF-κB p50		
sample	spiked (pM)	detected (pM)	RSD (%)	recovery (%)
1	0	65.54	N/A	N/A
2	5	70.31	1.85	95.4
3	10	75.42	2.12	98.8
4	50	117.21	2.54	100.4
5	200	268.56	1.56	101.5
6	500	580.37	2.04	103.0
7	1000	1051.71	1.89	98.6

https://dx.doi.org/10.1021/acsami.0c01243
ACS Appl. Mater. Interfaces 2020, 12, 11409−11418

assay. The recovery of the biosensor was ranged from 95.4 to 103.0%, and the RSD was in the range of 1.56−2.54%, which indicated that the ECL ratiometric biosensor was applicable in the multicomponent samples.

CONCLUSIONS

In summary, an ECL-RET-based dual-wavelength ratiometric electrochemiluminescence biosensor, with Au-g-C_3N_4 as a donor and Au@TAT as an acceptor, was fabricated to detect TF NF-κB p50. The proposed ratiometric biosensor presented an extremely high ECL-RET efficiency and provided a convenient and effective method with a detection limit of 5.8 pM (3σ) in the range of 10 pM−10 nM. In addition, DTNs as the skeleton of the ratiometric biosensor supplied a steady and reliable platform for the close contact between Au-g-C_3N_4 and Au@TAT, which could protect the signal free from the disturbance of nonspecific absorption of the binding protein and antibody. The ratiometric ECL changes were generated as the dsDNA-TF-antibody sandwich structure was constituted. Besides, the dual-wavelength ratiometric biosensor showed an excellent reproducibility and specificity for the determination of NF-κB p50, which also exhibited a huge potential for the assays of other binding proteins in clinical analysis by the alternation of the dsDNA binding sequence and introduction of the corresponding antibody.

ASSOCIATED CONTENT

Supporting Information

The Supporting Information is available free of charge at https://pubs.acs.org/doi/10.1021/acsami.0c01243.

^{1}H NMR of compound TAT (Figure S1), PAGE image of DTNs (Figure S2), ECL response for the modifications of donor and acceptor (Figure S3), UV−vis absorption spectra and fluorescence spectra of Au@TAT and COOH-Au@TAT (Figure S4), the characterization of the electrode (CV, EIS, and ECL response) for each modified steps (Figure S5), ECL-RET efficiency and comparison of the biosensor (Figure S6), dynamic light scattering results of TAT and Au@TAT (Figure S7), oligonucleotides sequences of the DTNs (Table S1), comparison of the performances of some transcription factor biosensors (Table S2) (PDF)

AUTHOR INFORMATION

Corresponding Authors

Jianfeng Zhao − *NHC Key Laboratory of Nuclear Medicine, Jiangsu Key Laboratory of Molecular Nuclear Medicine, Jiangsu Institute of Nuclear Medicine, Wuxi 214063, Jiangsu, China; Key Laboratory of Flexible Electronics (KLOFE) & Institute of Advanced Materials (IAM), Jiangsu National Synergetic Innovation Center for Advanced Materials (SICAM), Nanjing Tech University (NanjingTech), Nanjing 211816, P. R. China*; Phone: +86-510-85508775; Email: iamjfzhao@outlook.com

Kai Zhang − *NHC Key Laboratory of Nuclear Medicine, Jiangsu Key Laboratory of Molecular Nuclear Medicine, Jiangsu Institute of Nuclear Medicine, Wuxi 214063, Jiangsu, China; Department of Radiopharmaceuticals, School of Pharmacy, Nanjing Medical University, Nanjing 211166, China*; orcid.org/0000-0002-7021-5395; Email: zhangkai@jsinm.org

Wei Huang − *Key Laboratory of Flexible Electronics (KLOFE) & Institute of Advanced Materials (IAM), Jiangsu National Synergetic Innovation Center for Advanced Materials (SICAM), Nanjing Tech University (NanjingTech), Nanjing 211816, P. R. China; Shaanxi Institute of Flexible Electronics (SIFE), Northwestern Polytechnical University (NPU), Xi'an 710072, Shaanxi, P. R. China*; orcid.org/0000-0001-7004-6408; Email: iamwhuang@njtech.edu.cn

Authors

Zhenqiang Fan − *NHC Key Laboratory of Nuclear Medicine, Jiangsu Key Laboratory of Molecular Nuclear Medicine, Jiangsu Institute of Nuclear Medicine, Wuxi 214063, Jiangsu, China; Key Laboratory of Flexible Electronics (KLOFE) & Institute of Advanced Materials (IAM), Jiangsu National Synergetic Innovation Center for Advanced Materials (SICAM), Nanjing Tech University (NanjingTech), Nanjing 211816, P. R. China*

Zongqiong Lin − *Shaanxi Institute of Flexible Electronics (SIFE), Northwestern Polytechnical University (NPU), Xi'an 710072, Shaanxi, P. R. China*

Zepeng Wang − *Key Laboratory of Flexible Electronics (KLOFE) & Institute of Advanced Materials (IAM), Jiangsu National Synergetic Innovation Center for Advanced Materials (SICAM), Nanjing Tech University (NanjingTech), Nanjing 211816, P. R. China*

Jianfeng Wang − *Key Laboratory of Flexible Electronics (KLOFE) & Institute of Advanced Materials (IAM), Jiangsu National Synergetic Innovation Center for Advanced Materials (SICAM), Nanjing Tech University (NanjingTech), Nanjing 211816, P. R. China*

Minhao Xie − *NHC Key Laboratory of Nuclear Medicine, Jiangsu Key Laboratory of Molecular Nuclear Medicine, Jiangsu Institute of Nuclear Medicine, Wuxi 214063, Jiangsu, China; Department of Radiopharmaceuticals, School of Pharmacy, Nanjing Medical University, Nanjing 211166, China*

Complete contact information is available at: https://pubs.acs.org/10.1021/acsami.0c01243

Author Contributions

$^{\perp}$Z.F. and Z.L. contributed equally to this work.

Notes

The authors declare no competing financial interest.

ACKNOWLEDGMENTS

This work was supported by the National Natural Science Foundation of China (21705061, 21975126, 21875191), and China-Sweden Joint Mobility Project (No. 51811530018), the Natural Science Foundation of Jiangsu Province (BK20171470), Ministry of Education and Synergetic Innovation Center for Organic Electronics and Information Displays for financial support, the Jiangsu Provincial Key Medical Discipline (Laboratory) (ZDXKA2016017), and the Innovation Capacity Development Plan of Jiangsu Province (BM2018023).

REFERENCES

(1) Ma, X.; Ning, S. Shikimic Acid Promotes Estrogen Receptor-(ER)-Positive Breast Cancer Cells Proliferation via Activation of NF-kappa B Signaling. *Toxicol. Lett.* **2019**, *312*, 65−71.

(2) Fan, Z.; Wang, J.; Hao, N.; Li, Y.; Yin, Y.; Wang, Z.; Ding, Y.; Zhao, J.; Zhang, K.; Huang, W. Ultrasensitive Detection of Transcription Factors with A Highly-Efficient Diaminoterephthalate Fluorophore via An Electrogenerated Chemiluminescence Strategy. *Chem. Commun.* **2019**, *55*, 11892−11895.

(3) Zhong, Z.; Umemura, A.; Sanchez-Lopez, E.; Liang, S.; Shalapour, S.; Wong, J.; He, F.; Boassa, D.; Perkins, G.; Ali, S. R.; McGeough, M. D.; Ellisman, M. H.; Seki, E.; Gustafsson, A. B.; Hoffman, H. M.; Diaz-Meco, M. T.; Moscat, J.; Karin, M. NF-Kappa B Restricts Inflammasome Activation via Elimination of Damaged Mitochondria. *Cell* **2016**, *164*, 896−910.
(4) Zhang, Q.; Lenardo, M. J.; Baltimore, D. 30 Years of NF-kappa B: a Blossoming of Relevance to Human Pathobiology. *Cell* **2017**, *168*, 37−57.
(5) Liu, B.; Sun, L.; Liu, Q.; Gong, C.; Yao, Y.; Lv, X.; Lin, L.; Yao, H.; Su, F.; Li, D.; Zeng, M.; Song, E. A Cytoplasmic NF-kappa B Interacting Long Noncoding RNA Blocks I kappa B Phosphorylation and Suppresses Breast Cancer Metastasis. *Cancer Cell* **2015**, *27*, 370−381.
(6) Badis, G.; Berger, M. F.; Philippakis, A. A.; Talukder, S.; Gehrke, A. R.; Jaeger, S. A.; Chan, E. T.; Metzler, G.; Vedenko, A.; Chen, X.; Kuznetsov, H.; Wang, C.-F.; Coburn, D.; Newburger, D. E.; Morris, Q.; Hughes, T. R.; Bulyk, M. L. Diversity and Complexity in DNA Recognition by Transcription Factors. *Science* **2009**, *324*, 1720−1723.
(7) Gupta, S.; Cheng, H.; Mollah, A. K. M. M.; Jamison, E.; Morris, S.; Chance, M. R.; Khrapunov, S.; Brenowitz, M. DNA and Protein Footprinting Analysis of the Modulation of DNA Binding by the N-terminal Domain of the *Saccharomyces cerevisiae* TATA Binding Protein. *Biochemistry* **2007**, *46*, 9886−9898.
(8) Ranguelova, K.; Suarez, J.; Magliozzo, R. S.; Mason, R. P. Spin Trapping Investigation of Peroxide and Isoniazid-Induced Radicals in *Mycobacterium tuberculosis* Catalase-Peroxidase. *Biochemistry* **2008**, *47*, 11377−11385.
(9) Chung, M.; Kim, D.; Herr, A. E. Microchamber Western Blotting Using Poly-l-lysine Conjugated Polyacrylamide Gel for Blotting of Sodium Dodecyl Sulfate Coated Proteins. *Anal. Chem.* **2013**, *85*, 7753−7761.
(10) Tia, S. Q.; He, M.; Kim, D.; Herr, A. E. Multianalyte on-Chip Native Western Blotting. *Anal. Chem.* **2011**, *83*, 3581−3588.
(11) Kwon, S.; Cho, C. H.; Lee, E. S.; Park, J.-K. Automated Measurement of Multiple Cancer Biomarkers Using Quantum-Dot-Based Microfluidic Immunohistochemistry. *Anal. Chem.* **2015**, *87*, 4177−4183.
(12) Zeng, Z.; Cui, B.; Wang, Y.; Sun, C.; Zhao, X.; Cui, H. Dual Reaction-Based Multimodal Assay for Dopamine with High Sensitivity and Selectivity Using Functionalized Gold Nanoparticles. *ACS Appl. Mater. Interfaces* **2015**, *7*, 16518−16524.
(13) Bonnet, G.; Tyagi, S.; Libchaber, A.; Kramer, F. R. Thermodynamic Basis of the Enhanced Specificity of Structured DNA Probes. *Proc. Natl. Acad. Sci. U.S.A.* **1999**, *96*, 6171−6176.
(14) Zhu, S.; Lin, X.; Ran, P.; Xia, Q.; Yang, C.; Ma, J.; Fu, Y. A novel Luminescence-Functionalized Metal-Organic Framework Nanoflowers Electrochemiluminesence Sensor via "on-off" System. *Biosens. Bioelectron.* **2017**, *91*, 436−440.
(15) Pu, G.; Zhang, D.; Mao, X.; Zhang, Z.; Wang, H.; Ning, X.; Lu, X. Biomimetic Interfacial Electron-Induced Electrochemiluminesence. *Anal. Chem.* **2018**, *90*, 5272−5279.
(16) Muzyka, K.; Saqib, M.; Liu, Z.; Zhang, W.; Xu, G. Progress and Challenges in Electrochemiluminescent Aptasensors. *Biosens. Bioelectron.* **2017**, *92*, 241−258.
(17) Zhang, H.; Zhang, C.; Liu, D.; Zuo, F.; Chen, S.; Yuan, R.; Xu, W. A Ratiometric Electrochemiluminescent Biosensor for Con A Detecting Based on Competition of Dissolved Oxygen. *Biosens. Bioelectron.* **2018**, *120*, 40−46.
(18) Ding, C.; Li, Y.; Wang, L.; Luo, X. Ratiometric Electrogenerated Chemiluminescence Cytosensor Based on Conducting Polymer Hydrogel Loaded with Internal Standard Molecules. *Anal. Chem.* **2019**, *91*, 983−989.
(19) Huo, X.-L.; Zhang, N.; Yang, H.; Xu, J.-J.; Chen, H.-Y. Electrochemiluminescence Resonance Energy Transfer System for Dual-Wavelength Ratiometric miRNA Detection. *Anal. Chem.* **2018**, *90*, 13723−13728.
(20) Wu, L.; Ding, F.; Yin, W.; Ma, J.; Wang, B.; Nie, A.; Han, H. From Electrochemistry to Electroluminescence: Development and Application in a Ratiometric Aptasensor for Aflatoxin B1. *Anal. Chem.* **2017**, *89*, 7578−7585.
(21) Fu, X.; Tan, X.; Yuan, R.; Chen, S. A Dual-Potential Electrochemiluminescence Ratiometric Sensor for Sensitive Detection of Dopamine Based on Graphene-CdTe Quantum Dots and Self-Enhanced Ru(II) complex. *Biosens. Bioelectron.* **2017**, *90*, 61−68.
(22) Wang, Y.-Z.; Hao, N.; Feng, Q.-M.; Shi, H.-W.; Xu, J.-J.; Chen, H.-Y. A Ratiometric Electrochemiluminescence Detection for Cancer Cells Using g-C_3N_4 Nanosheets and Ag−PAMAM−Luminol Nanocomposites. *Biosens. Bioelectron.* **2016**, *77*, 76−82.
(23) Feng, X.; Gan, N.; Zhang, H.; Li, T.; Cao, Y.; Hu, F.; Jiang, Q. Ratiometric Biosensor Array for Multiplexed Detection of microRNAs Based on Electrochemiluminescence Coupled with Cyclic Voltammetry. *Biosens. Bioelectron.* **2016**, *75*, 308−314.
(24) Lei, Y.-M.; Huang, W.-X.; Zhao, M.; Chai, Y.-Q.; Yuan, R.; Zhuo, Y. Electrochemiluminescence Resonance Energy Transfer System: Mechanism and Application in Ratiometric Aptasensor for Lead Ion. *Anal. Chem.* **2015**, *87*, 7787−7794.
(25) Ye, J.; Zhu, L.; Yan, M.; Zhu, Q.; Lu, Q.; Huang, J.; Cui, H.; Yang, X. Dual-Wavelength Ratiometric Electrochemiluminescence Immunosensor for Cardiac Troponin I detection. *Anal. Chem.* **2019**, *91*, 1524−1531.
(26) Feng, Q.-M.; Shen, Y.-Z.; Li, M.-X.; Zhang, Z.-L.; Zhao, W.; Xu, J.-J.; Chen, H.-Y. Dual-Wavelength Electrochemiluminescence Ratiometry Based on Resonance Energy Transfer between Au Nanoparticles Functionalized g-C_3N_4 Nanosheet and $Ru(bpy)_3^{2+}$ for microRNA Detection. *Anal. Chem.* **2016**, *88*, 937−944.
(27) Gao, J.; Chen, Z.; Mao, L.; Zhang, W.; Wen, W.; Zhang, X.; Wang, S. Electrochemiluminescent Aptasensor Based on Resonance Energy Transfer System between CdTe Quantum Dots and Cyanine Dyes for the Sensitive Detection of Ochratoxin A. *Talanta* **2019**, *199*, 178−183.
(28) Fu, X.-L.; Hou, F.; Liu, F.-R.; Ren, S.-W.; Cao, J.-T.; Liu, Y.-M. Electrochemiluminescence Energy Resonance Transfer in 2D/2D Heterostructured g-C_3N_4/MnO_2 for Glutathione Detection. *Biosens. Bioelectron.* **2019**, *129*, 72−78.
(29) Wang, M.; Yin, H.; Zhou, Y.; Sui, C.; Wang, Y.; Meng, X.; Waterhouse, G. I. N.; Ai, S. Photoelectrochemical Biosensor for microRNA Detection Based on a MoS_2/g-C_3N_4/black TiO_2 Heterojunction with Histostar@AuNPs for Signal Amplification. *Biosens. Bioelectron.* **2019**, *128*, 137−143.
(30) Miao, L.; Jiao, L.; Tang, Q.; Li, H.; Zhang, L.; Wei, Q. A Nanozyme-Linked Immunosorbent Assay for Dual-Modal Colorimetric and Ratiometric Fluorescent Detection of Cardiac Troponin I. *Sens. Actuators, B* **2019**, *288*, 60−64.
(31) Liu, G.; Jin, B.-K.; Ma, C.; Chen, Z.; Zhu, J.-J. Potential-Resolved Electrochemiluminescence Nanoprobes for Visual Apoptosis Evaluation at Single-Cell Level. *Anal. Chem.* **2019**, *91*, 6363−6370.
(32) Christoffers, J. Diaminoterephthalate Fluorescence Dyes-Versatile Tools for Life Sciences and Materials Science. *Eur. J. Org. Chem.* **2018**, *2018*, 2366−2377.
(33) Wallisch, M.; Sulmann, S.; Koch, K.-W.; Christoffers, J. Bifunctional Diaminoterephthalate Fluorescent Dye as Probe for Cross-Linking Proteins. *Chem. - Eur. J.* **2017**, *23*, 6535−6543.
(34) Lin, Y.; Jia, J.; Yang, R.; Chen, D.; Wang, J.; Luo, F.; Guo, L.; Qiu, B.; Lin, Z. Ratiometric Immunosensor for GP73 Detection Based on the Ratios of Electrochemiluminescence and Electrochemical Signal Using DNA Tetrahedral Nanostructure as the Carrier of Stable Reference Signal. *Anal. Chem.* **2019**, *91*, 3717−3724.
(35) Li, N.; Wang, M.; Gao, X.; Yu, Z.; Pan, W.; Wang, H.; Tang, B. A DNA Tetrahedron Nanoprobe with Controlled Distance of Dyes for Multiple Detection in Living Cells and in Vivo. *Anal. Chem.* **2017**, *89*, 6670−6677.
(36) Nie, W.; Wang, Q.; Zou, L.; Zheng, Y.; Liu, X.; Yang, X.; Wang, K. Low-Fouling Surface Plasmon Resonance Sensor for Highly Sensitive Detection of microRNA in A Complex Matrix Based on the DNA Tetrahedron. *Anal. Chem.* **2018**, *90*, 12584−12591.
(37) Chen, X.; Huang, J.; Zhang, S.; Mo, F.; Su, S.; Li, Y.; Fang, L.; Deng, J.; Huang, H.; Luo, Z.; Zheng, J. Electrochemical Biosensor for

https://dx.doi.org/10.1021/acsami.0c01243
ACS Appl. Mater. Interfaces 2020, 12, 11409−11418

DNA Methylation Detection Through Hybridization Chain-Amplified Reaction Coupled with A Tetrahedral DNA Nanostructure. *ACS Appl. Mater. Interfaces* **2019**, *11*, 3745−3752.
(38) Song, P.; Li, M.; Shen, J.; Pei, H.; Chao, J.; Su, S.; Aldalbahi, A.; Wang, L.; Shi, J.; Song, S.; Wang, L.; Fan, C.; Zuo, X. Dynamic Modulation of DNA Hybridization Using Allosteric DNA Tetrahedral Nanostructures. *Anal. Chem.* **2016**, *88*, 8043−8049.
(39) Hu, J.; Liu, M.-H.; Zhang, C.-Y. Construction of Tetrahedral DNA-Quantum Dot Nanostructure with the Integration of Multistep Forster Resonance Energy Transfer for Multiplex Enzymes Assay. *ACS Nano* **2019**, *13*, 7191−7201.
(40) Pei, H.; Lu, N.; Wen, Y.; Song, S.; Liu, Y.; Yan, H.; Fan, C. A DNA Nanostructure-based Biomolecular Probe Carrier Platform for Electrochemical Biosensing. *Adv. Mater.* **2010**, *22*, 4754−4758.
(41) Pei, H.; Wan, Y.; Li, J.; Hu, H.; Su, Y.; Huang, Q.; Fan, C. Regenerable Electrochemical Immunological Sensing at DNA Nanostructure-Decorated Gold Surfaces. *Chem. Commun.* **2011**, *47*, 6254−6256.
(42) Qu, X.; Zhang, H.; Chen, H.; Aldalbahi, A.; Li, L.; Tian, Y.; Weitz, D. A.; Pei, H. Convection-Driven Pull-Down Assays in Nanoliter Droplets Using Scaffolded Aptamers. *Anal. Chem.* **2017b**, *89*, 3468−3473.
(43) Qu, X.; Yang, F.; Chen, H.; Li, J.; Zhang, H.; Zhang, G.; Li, L.; Wang, L.; Song, S.; Tian, Y.; Pei, H. Bubble-Mediated Ultrasensitive Multiplex Detection of Metal Ions in Three-Dimensional DNA Nanostructure-Encoded Microchannels. *ACS Appl. Mater. Interfaces* **2017**, *9*, 16026−16034.
(44) Xiao, M.; Lai, W.; Man, T.; Chang, B.; Li, L.; Chandrasekaran, A. R.; Pei, H. Rationally Engineered Nucleic Acid Architectures for Biosensing Applications. *Chem. Rev.* **2019**, *119*, 11631−11717.
(45) Su, Y.; Li, D.; Liu, B.; Xiao, M.; Wang, F.; Li, L.; Zhang, X.; Pei, H. Rational Design of Framework Nucleic Acids for Bioanalytical Applications. *ChemPlusChem* **2019**, *84*, 512−523.
(46) Feng, X.; Gan, N.; Zhang, H.; Yan, Q.; Li, T.; Cao, Y.; Hu, F.; Yu, H.; Jiang, Q. A Novel "Dual-Potential" Electrochemiluminescence Aptasensor Array Using CdS Quantum Dots and Luminol-Gold Nanoparticles as Labels for Simultaneous Detection of Malachite Green and Chloramphenicol. *Biosens. Bioelectron.* **2015**, *74*, 587−593.
(47) Kong, Y.; Shen, J.; Fan, A. Colorimetric Method for the Detection of Mercury Ions Based on Gold Nanoparticles and Mercaptophenyl Boronic Acid. *Anal. Sci.* **2017**, *33*, 925.
(48) Zhang, K.; Wang, K.; Zhu, X.; Xie, M. Sensitive Detection of Transcription Factors in Cell Nuclear Extracts by Using A Molecular Beacons Based Amplification Strategy. *Biosens. Bioelectron.* **2016**, *77*, 264−269.
(49) Zhang, Y.; Hu, J.; Zhang, C.-Y. Sensitive Detection of Transcription Factors by Isothermal Exponential Amplification-Based Colorimetric Assay. *Anal. Chem.* **2012**, *84*, 9544−9549.
(50) Xiong, Y.; Lin, L.; Zhang, X.; Wang, G. Label-Free Electrochemiluminescent Detection of Transcription Factors with Hybridization Chain Reaction Amplification. *RSC Adv.* **2016**, *6*, 37681−37688.
(51) Cheng, C.; Huang, Y.; Tian, X.; Zheng, B.; Li, Y.; Yuan, H.; Xiao, D.; Xie, S.; Choi, M. M. F. Electrogenerated Chemiluminescence Behavior of Graphite-Like Carbon Nitride and Its Application in Selective Sensing Cu^{2+}. *Anal. Chem.* **2012**, *84*, 4754−4759.

https://dx.doi.org/10.1021/acsami.0c01243
ACS Appl. Mater. Interfaces 2020, 12, 11409−11418